

Outflowing photoionized plasma in Circinus X-1 using the high-resolution X-ray spectrometer *Resolve* onboard XRISM and the radiative transfer code `cloudy`

Masahiro Tsujimoto,^{1,*} Teruaki Enoto,² María Díaz Trigo,³ Natalie Hell,⁴ Priyanka Chakraborty,⁵ Maurice A. Leutenegger,⁶ Michael Loewenstein,⁶ Pragati Pradhan,⁷ Megumi Shidatsu,⁸ Hiromitsu Takahashi,⁹ Tahir Yaqoob^{6,10,11}

¹Japan Aerospace Exploration Agency (JAXA), Institute of Space and Astronautical Science (ISAS), Chuo-ku, Sagami-hara, Kanagawa 252-5210, Japan

²Department of Physics, Graduate School of Science, Kyoto University, Sakyo-ku, Kyoto, Kyoto 606-8502, Japan

³European Southern Observatory, Garching bei München, Germany

⁴Lawrence Livermore National Laboratory, Livermore, CA 94550, USA

⁵Center for Astrophysics, Harvard & Smithsonian, Cambridge, MA 02138, USA

⁶NASA / Goddard Space Flight Center, Greenbelt, MD 20771, USA

⁷Department of Physics, Embry-Riddle Aeronautical University, Prescott, AZ 86301, USA

⁸Department of Physics, Ehime University, Matsuyama, Ehime 790-8577, Japan

⁹Department of Physics, Hiroshima University, Higashi-Hiroshima, Hiroshima 739-8526, Japan

¹⁰Center for Space Sciences and Technology, University of Maryland, Baltimore County (UMBC), Baltimore, MD 21250 USA

¹¹Center for Research and Exploration in Space Science and Technology, NASA / GSFC (CRESST II), Greenbelt, MD 20771, USA

¹²Department of Astronomy, University of Maryland, College Park, MD 20742, USA

*E-mail: tsujimoto.masahiro@jaxa.jp

ORCID: 0000-0002-9184-5556, 0000-0003-1244-3100, 0000-0001-7796-4279, 0000-0003-3057-1536, 0000-0002-4469-2518, 0000-0002-3331-7595, 0000-0002-1661-4029, 0000-0002-1131-3059, 0000-0001-8195-6546, 0000-0001-6314-5897

Abstract

High-resolution X-ray spectroscopy is a key to understanding the mass inflow and outflow of compact objects. Spectral lines carry information about the ionization, density, and velocity structures through their intensity ratios and profiles. They are formed in non-local thermodynamic equilibrium conditions under the intense radiation field from the compact objects, thus radiative transfer (RT) calculation is a requisite for proper interpretations. We present such a study for a low-mass X-ray binary, Circinus X-1, from which the P Cygni profile was discovered using the X-ray grating spectrometer onboard Chandra. We observed the source using the X-ray microcalorimeter onboard XRISM at an orbital phase of 0.93–0.97 and revealed many spectral features unidentified before; the higher series transitions ($n \rightarrow 1$; $n > 2$) of highly-ionized (H- and He-like) S, Ca, Ar, and Fe in emission and absorption, the Fe $K\alpha$ and $K\beta$ inner-shell excitation absorption of mildly-ionized (O- to Li-like) Fe, and resolved fine-structure level transitions in the Fe $Ly\alpha$ and He α complexes. They blend with each other at different velocity shifts on top of apparently variable continuum emission that changed its flux by an order of magnitude within a 70 ks telescope time. Despite such complexity in the observed spectra, most of them can be explained by a simple model consisting of the photoionized plasma outflowing at $\sim 300 \text{ km s}^{-1}$ and the variable blocking material in the line of sight of the incident continuum emission from the accretion disk. We demonstrate this with the aid of the RT code `cloudy` for the line ratio diagnostics and spectral fitting. We further constrain the physical parameters of the outflow and argue that the outflow is launched close to the outer edge of the accretion disk and can be driven radiatively by being assisted by the line force calculated using the RT simulation.

Keywords: radiative transfer — stars: neutron — techniques: spectroscopic — X-rays: binaries

1 Introduction

Compact objects, such as black holes (BH) and neutron stars (NS), are a cosmic pumping mechanism of mass, momentum, and energy. A part of the accreted matter onto the compact objects, such as those in X-ray binaries and at the center of galaxies, is ejected in the form of jets and winds. They carry momentum and energy concentrated in a fraction of accreted mass, through which the redistribution of momentum and energy takes place in the universe.

High-resolution X-ray spectroscopy is one of the best observa-

tional tools to unveil such an outflowing mass. Because of the strong radiation field of compact objects, the matter around them is often photoionized. Copious emission lines from the photoionized plasma, as well as absorption lines imprinted in the continuum emission transmitted through it, are routinely observed in such systems. They carry information on the ionization, density, and velocity structures of matter around compact objects.

With the advent of the X-ray microcalorimeter (*Resolve*; Ishisaki et al. 2022) onboard the X-Ray Imaging and Spectroscopy Mission (XRISM; Tashiro et al. 2020), new spectral features be-

came available for diagnosing these photoionized plasmas. They are particularly rich in the Fe K band (6–9 keV), which includes the Fe K α line from neutral to low-ionized (up to Ne-like) ions, the inner-shell excitation lines from mildly-ionized (F-like to Li-like) ions, fine-structure lines of He α and Ly α ($n = 2 \rightarrow 1$) line complexes from highly-ionized (He- and H-like) ions, and their higher series counterparts ($n \rightarrow 1$; $n > 2$).

The intensity ratios of these lines provide robust constraints for plasma parameters. For this purpose, it is mandatory to consult the radiative transfer (RT) calculations. In photoionized plasmas, the lines are formed in non-local thermodynamic equilibrium (NLTE) conditions, in which radiative processes dominate the heating/cooling, ionization/recombination, and excitation/deexcitation balances over collisional processes. Matter and photons are only weakly coupled, and the radiation field is far from blackbody. For the line ratio diagnostics, we need to know the charge and level populations of matter by solving all the matter-photon interactions consistently with the radiation field through numerical RT calculations.

In systems of our interest, two RT effects (continuum pumping and line optical depth) are of particular importance. Depending on their combinations, they are labeled as case A (lines are optically thin, no continuum pumping), B (optically thick, no continuum pumping), C (optically thin, with continuum pumping), and D (optically thick, with continuum pumping). See Chakraborty et al. (2021) and references therein for more details.

The first is the continuum pumping, in which incident continuum photons radiatively excite matter. Lines with a large oscillator strength are strongly enhanced in observed spectra if a part of the incident emission is blocked in the line of sight, which is indeed observed in Seyfert 2 galaxies (Kinkhabwala et al. 2002), accretion disk corona sources (Tsujiimoto et al. 2024), and eclipsing binaries during eclipse (Wojdowski et al. 2003).

The second is the line optical depth. At the line center energy, the optical depth is given by

$$\tau_0 = \frac{1}{4\pi\epsilon_0} \frac{\pi e^2}{m_e c} f \frac{1}{\sqrt{\pi}\Delta\nu_D} N_H A_Z A_C A_L, \quad (1)$$

in which $\Delta\nu_D \equiv \frac{E_0}{hc} \sqrt{\frac{2k_B T}{m_Z} + v_{\text{turb}}^2}$ is the line width, E_0 is the energy of the line, f is the oscillator strength, A_Z is the abundance of the element Z relative to H, A_C is the fractional charge population of Z^{C+} , A_L is the fractional level population of the level L , m_Z is the atomic mass of Z , T is the plasma temperature, v_{turb} is the turbulent velocity, and other symbols follow their conventions. To take the Fe XXVI Ly α_1 line ($^2P_{3/2} \rightarrow ^2S_{1/2}$) as an example, $E_0 = 6.973$ keV (Yerokhin & Surzhykov 2019), $f = 0.27$ (Fuhr et al. 1988), $A_{\text{Fe}} = 2.7 \times 10^{-5}$ (Wilms et al. 2000), $A_{26} = 0.5$, $A_{(1s)} = 1.0$, and $T = 10^6$ K, we obtain $\tau_0 = 1$ for $N_H = 1.7 \times 10^{21}$ cm $^{-2}$. Many systems have larger N_H values. The situation approaches to case B or D, which are manifested by a higher Lyman series photon ($n \rightarrow 1$; $n > 2$) degrading into a Balmer series ($n \rightarrow 2$; $n > 2$) photon and a Ly α ($n = 2 \rightarrow 1$) photon or by two photon decay after repeating numerous resonance scattering due to their large optical depth (Menzel & Baker 1937).

In general, RT effects depend on the geometry, density and velocity structures, and the spectral shape of the incident emission. Generic tools widely used in X-ray spectroscopy are not universally applicable to all systems. Calculations specific to each system are necessary and should be the norm in the X-ray microcalorimeter era that has just begun. Also, in practice, numerous lines appear both in emission and absorption, blending each other and being shifted by different redshifts, in high-resolution X-ray

spectra as we will show in this paper. Synthesized spectra with RT calculations are needed to disentangle such complexities. This is clearly demonstrated in the X-ray microcalorimeter data of Cyg X-3 (XRISM Collaboration et al. 2024).

The purpose of this paper is to showcase the utility of the RT calculation in interpreting the microcalorimeter data, focusing on line ratios, and thereby constraining the physics of the mass outflow from compact objects. We use a low-mass X-ray binary Circinus X-1 (Cir X-1), which was observed with XRISM showing particularly rich spectral features, thus is challenging for modeling. We use the *c*loudy code for the RT calculation. We start with a brief description of the source and why we chose it for our study in §2. We present the observation and data reduction in §3. We give a phenomenological description of the spectrum in §4. We conduct the RT calculation and perform line ratio diagnostics as well as spectral modeling in §5. Based on these, we discuss the physical parameters and the driving mechanism of the outflow in §6. The conclusion is given in §7.

2 Target

Cir X-1 was discovered at the dawn of X-ray astronomy using an Aerobee 150 rocket (Margon et al. 1971). Since then, the source has been monitored in the X-rays for half a century, revealing its wild behavior in the flux that varies between a few milli and a super crab (Parkinson et al. 2003), which is unseen in any other X-ray binaries. There has been long debates on the nature of the enigmatic source, but accumulating evidence favors that it is a low-mass X-ray binary (LMXB) hosting a NS seen close to an edge-on view with an inclination angle of 60–75 degree (Tominaga 2024).

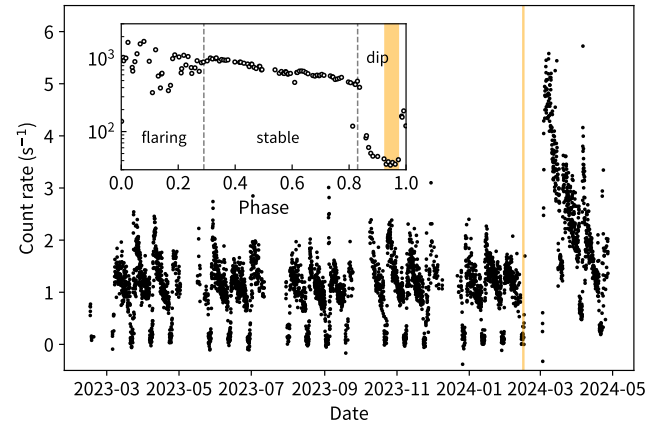


Fig. 1. X-ray light curve in the 2–20 keV band using the Gas Slit Cameras (Mihara et al. 2011) onboard MAXI (Matsuoka et al. 2009) for one year before the XRISM observation (orange) and a few months thereafter. The inset is the phase-folded light curve of the NICER observation covering an entire orbital phase in August 2020 (Tominaga et al. 2023). Two cycles after the XRISM observation, the flux increased, reaching the highest level since 2014. Alt text: two scatter plots of X-ray light curve of MAXI and NICER.

The binary has an orbital period of 16.6 day (Kaluzienski et al. 1976) with a large eccentricity of ~ 0.45 (Jonker et al. 2007) at a distance of 9.4 kpc (Heinz et al. 2015). This is one of a few known compact objects in a binary system associated with a supernova remnant that gave birth to the object, suggesting an extreme youth of $\sim 5 \times 10^3$ years (Heinz et al. 2013). Despite its youth, the NS is

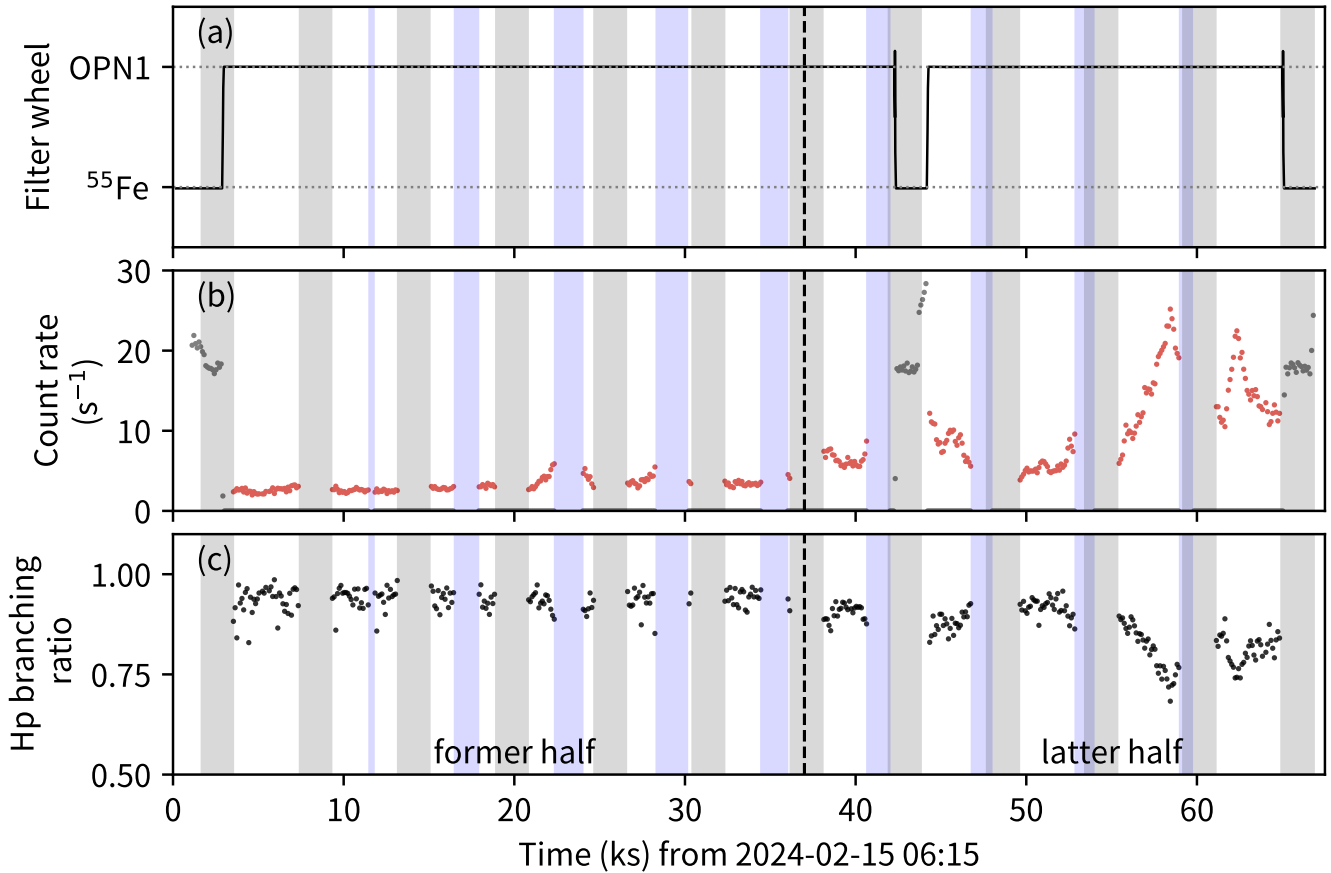


Fig. 2. (a) Filter wheel positions, (b) 2–12 keV count rate binned at 100 s, and (c) the fraction of Hp events. The count rate increased during the FW illumination (gray dots), which was not used except for gain tracking purposes. The observation was interrupted by South Atlantic Anomaly passages (blue) and the occultations by the Earth (gray). The observation is divided into two halves (18.1 and 16.8 ks each) by the broken line for time-sliced spectroscopy. Alt text: three scatter plots of filter wheel position, X-ray count rate, and the high primary branching ratio.

considered to have a weak magnetic field, which is evidenced by the lack of coherent X-ray signals, typical behaviors as a Z source (Shirey et al. 1998), the presence of twin kHz quasi-periodic oscillations (Boutloukos et al. 2006), and type I bursts (Tennant et al. 1986), all of which are observational signatures of LMXBs hosting a NS of a weak magnetic field (van der Klis 2006).

The source was observed with the High-Energy Transition Grating (HETG) spectrometer (Canizares et al. 2005) onboard the Chandra X-ray Observatory (Weisskopf et al. 2000) in the first year of launch when Cir X-1 was historically bright, exceeding a crab. The X-ray spectrum taken at the orbital phase $\phi = 0.99$ was rich in spectral features of highly-ionized Ne, Mg, Si, S, and Fe with a P Cygni profile of a velocity dispersion of $2 \times 10^3 \text{ km s}^{-1}$ (Brandt & Schulz 2000; Schulz & Brandt 2002). This was the first clear detection of the P Cygni profile in X-rays, which constitutes strong evidence for the presence of outflow. This was interpreted as outflows from the accretion disk (Brandt & Schulz 2000) and opens an avenue for constraining the physical parameters of the outflowing matter from compact objects through X-ray spectroscopy. However, HETG was sensitive to the P Cygni profile of the highest end of the velocity dispersion exceeding $\mathcal{O}(10^3 \text{ km s}^{-1})$ if we use highly-ionized Fe features, and the rest was left for microcalorimeter spectrometers.

The X-ray spectrum of Cir X-1 changes drastically along the orbital phase. During a decade-long low flux state in 2010's, the

change was non-repeatable (Asai et al. 2014). Since around July 2019, the flux has recovered to a few tenths of a crab and the orbital change has become repeatable, which continued until the XRISM observation (figure 1). Tominaga et al. (2023) conducted X-ray observations with the Neutron Star Interior Composition Explorer (NICER; Gendreau et al. 2016) that covered the entire orbital phase at high cadence in August 2020. They confirmed three phases based on flux variation (figure 1 inset) proposed earlier (Iaria et al. 2001); the dip phase ($\phi = 0.84 - 1.0$) when the flux decreases to a few percent, the flaring phase ($\phi = 0.0 - 0.29$) when the flux exhibits rapid variability, and the stable phase ($\phi = 0.29 - 0.83$) when the flux gradually declines. X-ray spectra were quite different among the phases or even within the same phase, but they were explained by the same phenomenological model with different parameters. The major factor for the variability was found to be the column density and the partial covering fraction of the absorber in the line of sight (Brandt et al. 1996). Emission and absorption features from the photoionized plasma were also found. The line ratios were stable over the phase despite the apparent change in the continuum flux. Based on this, Tominaga et al. (2023) came to a picture shown in their figure 6, based on which we will develop our interpretation of the XIRSM data to be shown below.

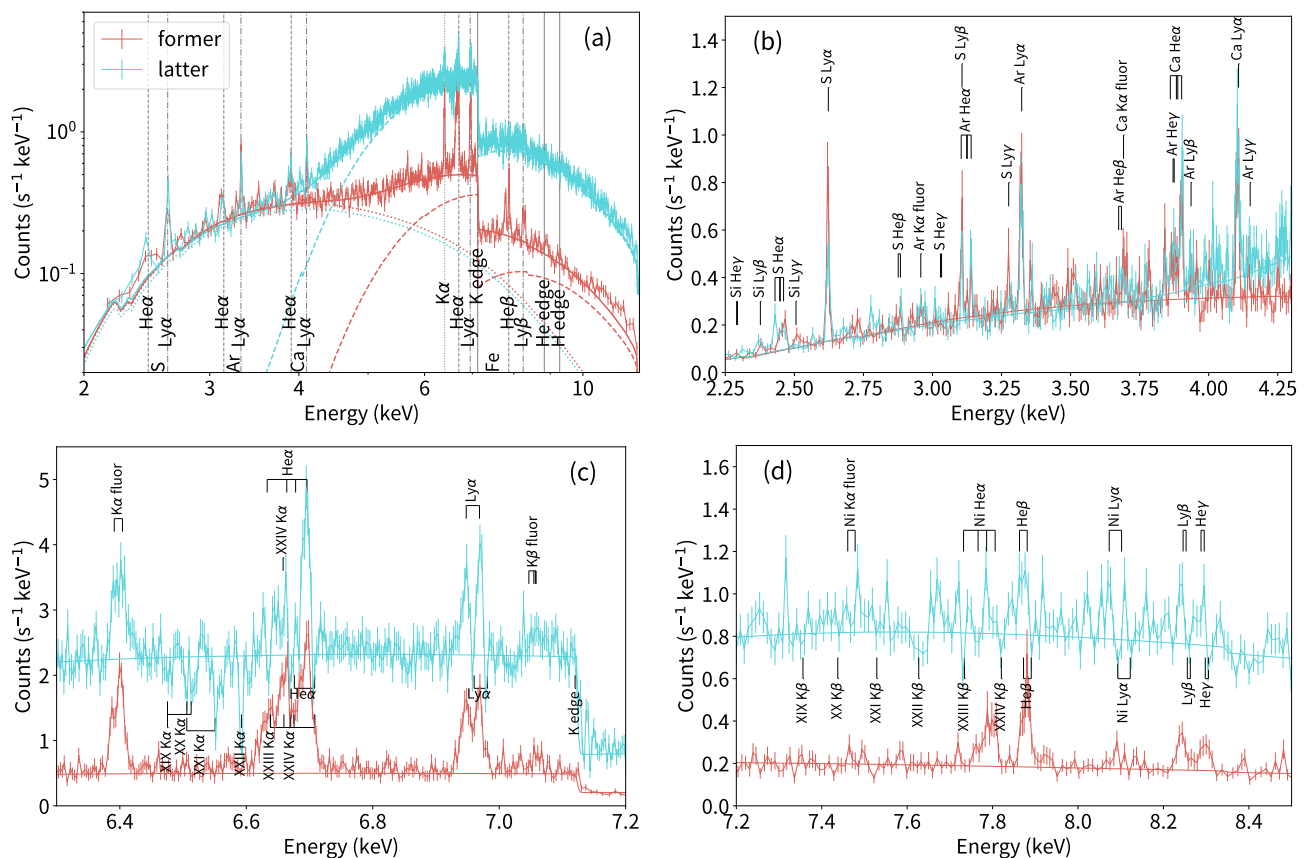


Fig. 3. (a) Total (2–12 keV), (b) soft (2.25–4.25 keV), (c) Fe $K\alpha$ (6.3–7.2 keV), and (d) Fe $K\beta$ (7.2–8.5 keV) band spectra of the former (red) and latter (cyan) half of the observation. The absorption lines are multiplicative and the emission lines are additive upon the continuum emission, thus their variations can be better viewed respectively in the logarithmic (a) and the linear (b–d) scale. The best-fit continuum model is shown: total (solid), absorbed (dotted) and unabsorbed (dashed) by the partial covering absorber. (b–d) Emission line complexes are shown on the upper side, while absorption line complexes are on the lower side of the data. Lines without an element name are Fe. The line labels are shifted by representative velocities for clarity: $+750 \text{ km s}^{-1}$ for Ni $Ly\alpha$ $+360 \text{ km s}^{-1}$ for the other Fe and Ni emission lines except for the fluorescence line, null for the other emission lines, and -180 km s^{-1} for all the absorption lines. Alt text: four line plots of X-ray spectra in different energy bands.

3 Observations and Data Reduction

3.1 Observation

The observation (sequence number 300028010) was made from 2024-02-15 06:19 to 2024-02-16 00:51 as a performance verification program. The duration covers an orbital phase of $\phi = 0.926$ – 0.973 in the ephemeris by Nicolson (2007). We targeted just before the phase origin $\phi = 0.0$ in the last part of the dip phase (figure 1 inset), which interested us the most among the NICER data covering an entire orbit (Tominaga et al. 2023).

In this paper, we focus on the *Resolve* data. The bandpass is limited to above $\sim 1.7 \text{ keV}$ due to the cryostat window yet to be opened (Midooka et al. 2021). Figure 2 shows the time series of some selected house keeping and X-ray event data. During the $\sim 70 \text{ ks}$ telescope time, the observation was interrupted by South Atlantic Anomaly (SAA) passages and occultation by the Earth. No recycling operation of the adiabatic demagnetization refrigerator was performed (Shirron et al. 2024). At the beginning, middle, and end of the observations, the filter wheel (Shipman et al. 2024) was rotated to illuminate the microcalorimeter pixels with the ^{55}Fe sources for gain tracking calibrations (Porter et al. 2016). Otherwise, the filter wheel was at an open position. The total on-source integration is 33.7 ks.

3.2 Data reduction

We started with the level 2 products of the pipeline processing (Doyle et al. 2022) version 03.00.011.008. The standard processing is adequate for this source in the right dynamic range of the count rate of $\mathcal{O}(10 \text{ s}^{-1})$; the background is negligible (Kilbourne et al. 2018) and artifacts due to high count rates are minimum (Mizumoto et al. 2022). We selected Hp grade events. Here, the Hp grade is given for events without any other events overlapping in time in the same pixel, which is well calibrated for energy as of writing. We also removed events below 0.3 keV, those with too fast or slow pulse rise times for their energy (Mochizuki et al. 2024), and those recorded with pixel 27, which is known to behave unpredictably in gain variation. A total of 0.2 million events were left.

During the observation, the count rate varied (figure 1b) and so did the Hp grade branching ratio as a result (figure 1c). Their average values are 6.4 s^{-1} and 0.86. The detector and telescope response files were generated for the observation duration of interest when spliced respectively using the `rs1mkrmf` and `xaarfgen` tools in the `HEASOFT` package version 6.34. The background spectrum was not subtracted. Pixel-to-pixel spectral variation of unidentified reasons is known, which may affect the global fitting results, but not the results based on line ratios. The errors quoted hereafter

represent a statistical uncertainty of 1σ .

4 Analysis

The goal of this section is to describe the spectrum using phenomenological models. We start by visually inspecting the data to identify spectral features and components (§4.1) and describe each component (§4.2) separately for the continuum (§4.2.1), emission lines (§4.2.2), and absorption lines (§4.2.3).

4.1 Inspection

The X-ray count rate is variable by an order of magnitude during the observation (figure 2b). The behavior is different in the former and the latter half. The X-ray spectrum is also different between the two halves. Figure 3 (a) shows the 2–12 keV band spectrum for the two halves. At least, two spectral components are recognized; the soft component is dominant below ~ 4 keV and is non-variable, while the hard component is dominant above ~ 4 keV and is variable.

The soft component (figure 3b) is characterized by emission lines of highly-ionized S, Ar, and Ca of $n = \{2, 3, 4\} \rightarrow 1$ transitions, which we respectively denote as Ly α , Ly β , and Ly γ for the H-like and He α , He β , and He γ for the He-like ions. The same component may account for the emission lines of highly-ionized Fe above ~ 4 keV for the $n = 2 \rightarrow 1$ transitions (figure 3c) and the $n = \{3, 4\} \rightarrow 1$ transitions (figure 3d) as well as the emission lines of highly-ionized Ni for the $n = 2 \rightarrow 1$ transitions (figure 3d).

The hard component suffers strong absorption by neutral matter, which is evident as the gradual attenuation toward the soft end and the photoionization K edge of Fe at 7.12 keV. The gradual attenuation is likely due to partial coverage by the neutral matter, as the attenuation toward the soft end is not as rapid as complete blocking. The depth of the Fe K edge is similar between the former and the latter half in the logarithmic scale (figure 3a), indicating that the absorbing column did not change much.

In the latter half of the observation, the hard component also suffers absorption by mildly-ionized Fe for the K α ($n = 2 \rightarrow 1$) and K β ($n = 3 \rightarrow 1$) transitions respectively in the 6.4–6.7 keV (figure 3c) and 7.3–7.9 keV (figure 3d) band. These are caused by the inner-shell excitation absorption from the ground state to excited levels of mildly ionized ions. The photoelectric absorption cross section exhibits strong resonance structures at these energies (Behar & Netzer 2002; Bautista et al. 2004; Kallman et al. 2004). Some hints of such absorption features were obtained in the HETG observations (Schulz et al. 2008) for the K α lines, which were clearly identified with *Resolve*. The new detection of the K β absorption lines is a consequence of two unique capabilities of *Resolve* besides the energy resolution: (i) its high quantum efficiency beyond 8 keV due to the HgTe X-ray absorber as opposed to the Si absorber in the conventional X-ray spectrometers and (ii) a very low background equivalent to only one event per spectral bin per 100 ks that allows detection of continuum emission with a high signal-to-noise ratio, upon which the absorption features are imprinted.

For the $n = \{2, 3, 4\} \rightarrow 1$ transitions of highly-ionized Fe, the features appear only in emission in the former half but appear both in emission and absorption in the latter half (figure 3c and d). The emission features are red-shifted, while the absorption features are blue-shifted, forming a P Cygni profile. This is evident in the w line at 6.700 keV in the He α complex and the Ly α_1 and Ly α_2 lines respectively at 6.973 and 6.952 keV in the Ly α complex. Here,

we use $^1P_1 \rightarrow ^1S_0$, $^3P_{1,2} \rightarrow ^1S_0$, and $^3S_1 \rightarrow ^1S_0$ transitions as w , x , y , and z lines in the He complex and $^2P_{3/2} \rightarrow ^2S_{1/2}$ and $^2P_{1/2} \rightarrow ^2S_{1/2}$ transitions as Ly $_1$ and Ly $_2$ lines in the Ly complex. These fine-structure levels were resolved with the *Resolve*'s energy resolution for the first time in space except for the Sun (Tanaka 1986).

By continuing the visual inspection, we can further deduce that the emission lines of the highly ionized Fe do not suffer from the absorption causing the Fe K edge at 7.12 keV. This is suggested from the Lyman decrement of H-like Fe; i.e. the line ratio between Fe Ly β at 8.25 keV over Ly α at 7.0 keV. The Ly β line is above and the Ly α line is below the Fe K edge. The face value of the Lyman decrement is ~ 0.2 in the former half of the spectrum. If we correct for the absorption represented by the Fe K edge, assuming that the Ly β emission line was attenuated by it, the corrected Lyman decrement would be ~ 1.0 , which cannot be achieved under any plasma conditions as we show later in §5.1.

4.2 Description

4.2.1 Continuum

For the phenomenological description of the spectra, we start with the continuum emission. We follow the approach in Tominaga et al. (2023), in which the broad-band spectrum is described by the partially-covered multi-color disk blackbody emission. The simple model successfully explained the varying spectra taken over an entire orbital phase with NICER.

We applied the model both for the former and the latter spectra in energy ranges devoid of spectral lines. The fitting parameters are the innermost temperature (T_{in}) and the normalization ($N^{(\text{disk})}$) of the disk blackbody emission, the H-equivalent column density ($N_{\text{H}}^{(\text{pca})}$), the covering fraction ($f^{(\text{pca})}$), and the Fe abundance ($A_{\text{Fe}}^{(\text{pca})}$) of the partial covering absorber (PCA). The Fe abundance parameter is intended to adjust for the Fe K edge depth. The entire spectrum is attenuated by the interstellar matter (ISM) of the H-equivalent column density ($N_{\text{H}}^{(\text{ism})}$). We tied the $N_{\text{H}}^{(\text{ism})}$, $A_{\text{Fe}}^{(\text{pca})}$, and T_{in} values common and others independent between the two spectra. This resulted in a reasonable fit with a reduced $\chi^2/\text{d.o.f} = 1.04/2483$. The best-fit parameters are shown in table 1 and the model in figure 3.

Table 1. Best-fit parameters for the continuum emission.

Comp	Par	Unit	Former	Latter
Disk*	T_{in}	(keV)	2.12 $^{+0.04}_{-0.04}$	
	$N^{(\text{disk})}$		3.88 $^{+0.52}_{-0.46}$	16.0 $^{+1.7}_{-1.6}$
PCA†	$N_{\text{H}}^{(\text{pca})}$	(10 22 cm $^{-2}$)	95.9 $^{+4.3}_{-4.2}$	74.1 $^{+1.4}_{-1.3}$
	$f^{(\text{pca})}$		0.91 $^{+0.01}_{-0.01}$	0.979 $^{+0.001}_{-0.001}$
	$A_{\text{Fe}}^{(\text{pca})}$		0.99 $^{+0.03}_{-0.03}$	
ISM†	$N_{\text{H}}^{(\text{ism})}$	(10 22 cm $^{-2}$)	0.98 $^{+0.25}_{-0.24}$	

* The *diskbb* model (Mitsuda et al. 1984) of *xspec* is used. The normalization is scaled as $N^{(\text{disk})} \equiv (R_{\text{in}}/D_{10})^2 \cos\theta$, in which R_{in} is the inner disk radius (km), D_{10} is the distance in the unit of 10 kpc, and θ is the viewing angle of the disk.

† The *tbpcf* model for PCA and *tbabs* model for ISM (Wilms et al. 2000) is used.

As expected, the absorbed and non-absorbed components by the PCA respectively account for the continuum emission below and above ~ 4 keV. The spectral change above 4 keV is mostly caused by the increase of $N^{(\text{disk})}$ by ~ 4 times, while the other parameters change much less of $\lesssim 20\%$. The flux of the non-absorbed component can be assessed with $N^{(\text{disk})}(1 - f^{(\text{pca})})$, which remained

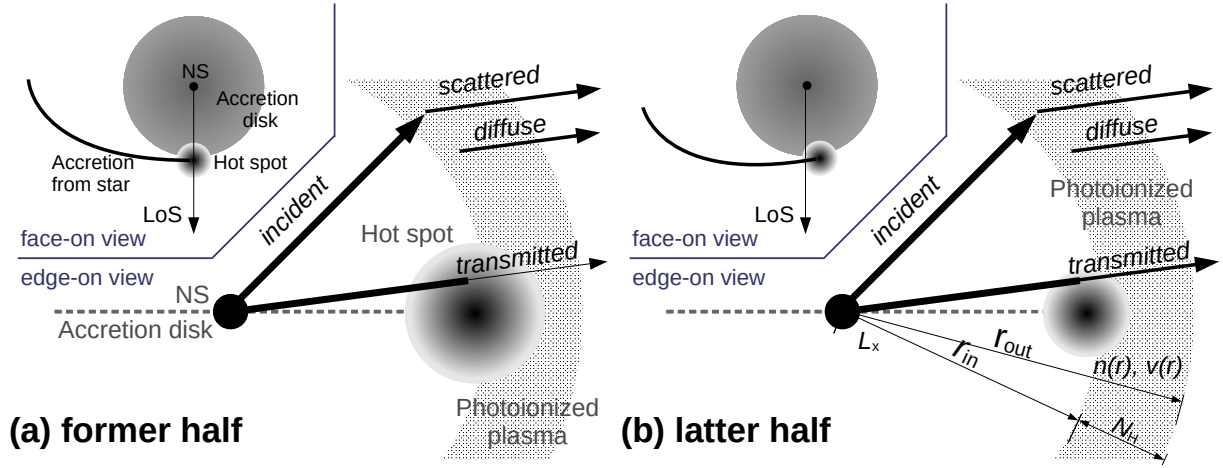


Fig. 4. Schematic view of the system for the photoionized plasma. The face-on (inset) and edge-on (main) views of the (a) former and (b) latter half of the observation are shown. The main difference is the clocking of the hot spot in the face-on view as the orbital phase progresses. This makes the change in the blocking fraction of the incident emission by the hot spot in the line of sight (LoS). The physical parameters used in the RT modeling is shown in (b). Alt text: two schematic views of the system for the former and the latter half of the observation.

the same within the error between the two spectra despite their independence in the fitting. The Fe K edge at 7.12 keV is fully explained by the PCA for $A_{\text{Fe}}^{\text{(pca)}}$ being consistent with unity.

4.2.2 Emission lines

We derive phenomenological parameters of emission line features using the former half of the spectrum, which is less contaminated by absorption features. We focus on conspicuous lines, including the Ly α line complex of S, Ar, Ca, Fe, and Ni and the Ly β complex of Fe for the H-like ions and the He α line complex of S, Ar, Ca, Fe, and Ni and the He β complex of Fe for the He-like ions. We also include the Fe K α fluorescence line complex.

For the Ly α and Ly β complexes, we applied two Gaussian models representing the Ly $_1$ and Ly $_2$ lines plus the power-law model representing the local underlying continuum. The intensity ratio of the two lines was fixed to 2:1. Their normalization, width, and redshift were fitted collectively for each complex. The exception is the Fe Ly α line, which has sufficient statistics to determine line normalization and width independently. For the He α and He β complexes, we used four Gaussian models representing the w , x , y , and z lines plus the power-law model. The intensity of the lines was fitted individually, while the redshift and the line width were fitted collectively for each complex. For the Fe K α fluorescence line, we used two Gaussian models instead of a more elaborate model (Hölzer et al. 1997) for simplicity. Table 2 shows the result.

4.2.3 Absorption lines

We describe the absorption features using the latter half of the observation. We see absorption lines of K α ($n = 2 \rightarrow 1$) transitions of Fe XIX–XXVI in the 6.45–7.05 keV (figure 3c) band and their K β ($n = 3 \rightarrow 1$) counterparts in the 7.2–8.2 keV band (figure 3d). The lines except for Fe XXV and Fe XXVI are formed by the inner-shell excitation transitions from the ground state to an excited state. There are numerous allowed transitions between them, but only a fraction is registered in the current atomic databases. We refer to *chianti* version 10.1 (Del Zanna et al. 2021), which has more entries than *AtomDB* version 3.0.9 (Smith et al. 2001; Foster & Heuer 2020) for the K α transitions. None is available for the K β transitions in both. We further restricted ourselves to using lines with

Table 2. Phenomenological model fitting for the emission lines in the former half.

Label	E^* (keV)	$\log f^\dagger$	I^\ddagger ($\text{ks}^{-1} \text{cm}^{-2}$)	v^\S (km s^{-1})
S XV He α (w)	2.461	−0.12	0.07 ± 0.02	-336 ± 70
S XVI Ly α_1	2.623	−0.56	0.14 ± 0.02	75 ± 49
Ar XVII He α (w)	3.140	−0.12	0.02 ± 0.01	-179 ± 41
Ar XVI Ly α_1	3.323	−0.56	0.06 ± 0.01	49 ± 59
Ca XIX He α (w)	3.902	−0.12	0.04 ± 0.01	103 ± 83
Ca XX Ly α_1	4.108	−0.56	0.04 ± 0.01	26 ± 45
Fe fluor K α_1	6.404	...	$0.12_{-0.01}^{+0.01}$	75 ± 27
Fe fluor K α_2	6.391	...	$0.07_{-0.01}^{+0.01}$	(tied w. above)
Fe XXV He α (w)	6.700	−0.14	0.28 ± 0.01	282 ± 23
Fe XXV He α (x)	6.682	−4.80	0.00 ± 0.00	(tied w. above)
Fe XXV He α (y)	6.668	−1.20	0.22 ± 0.01	(tied w. above)
Fe XXV He α (z)	6.637	−6.50	0.12 ± 0.01	(tied w. above)
Fe XXV He β (w)	7.881	−0.86	0.03 ± 0.01	(unconstrained)
Fe XXVI Ly α_1	6.973	−0.56	0.12 ± 0.01	237 ± 26
Fe XXVI Ly α_2	6.952	−0.87	0.11 ± 0.01	(tied w. above)
Fe XXVI Ly β_1	8.253	−1.30	0.02 ± 0.00	299 ± 74
Ni XXVII He α (w)	7.806	−0.15	0.03 ± 0.01	90 ± 76
Ni XXVIII Ly α_1	8.102	−0.56	0.01 ± 0.00	447 ± 276

* Energy from the *AtomDB* database (Smith et al. 2001; Foster & Heuer 2020).

† Logarithm of the oscillator strength from the upper to lower level for highly-ionized ions from the *AtomDB* database (Smith et al. 2001; Foster & Heuer 2020).

‡ Line intensity from the fitting.

§ Energy shift from the fitting. The redward shift is positive.

an experimentally verified wavelength for a reliable energy shift determination.

Upon the best-fit continuum (§ 4.2.1) and the emission line (§ 4.2.2) models, we multiplied a Gaussian absorption line for the transitions expected from the RT simulation described later (§ 5.1.2). We derived the best-fit optical depth individually for each line except for the Ly α doublet fixed to a 2:1 ratio. We derived the energy shift collectively as $-249_{-16}^{+16} \text{ km s}^{-1}$ for Fe XXV and XXVI and $-343_{-10}^{+10} \text{ km s}^{-1}$ for the remainder. The result is given in table 3.

Table 3. Phenomenological model fitting for the absorption lines in the latter half.

Label*	E^\dagger (keV)	Fe	Upper level ‡	$B_r(k, i)^\S$	τ^\parallel
(outer-shell transitions)					
Ly α_1	6.9732	XXVI	2p $^2P_{3/2}$	1	$0.29^{+0.05}_{-0.04}$
Ly α_2	6.9520	XXVI	2p $^2P_{1/2}$	1	(tied w. above)
w	6.7005	XXV	1s2p 1P_1	1	$0.27^{+0.05}_{-0.05}$
(inner-shell transitions)					
q	6.6622	XXIV	1s2s2p $^2P_{3/2}$	1.00	$0.45^{+0.07}_{-0.06}$
r	6.6528	XXIV	1s2s2p $^2P_{1/2}$	0.88	$0.37^{+0.05}_{-0.04}$
E1	6.6288	XXIII	1s2s 2p 1P_1	0.75	$0.04^{+0.04}_{-0.04}$
B	6.5861	XXII	1s2s $^2p^2$ $^2P_{1/2}$	0.63	$0.71^{+0.11}_{-0.08}$
			1s2s $^2p^2$ $^2D_{3/2}$	0.46	(blend w. above)
C1	6.5442	XXI	1s2s $^2p^3$ 3D_1	0.36	$0.46^{+0.07}_{-0.07}$
N2	6.5068	XX	1s2s $^2p^4$ $^4P_{3/2}$	0.29	$0.16^{+0.05}_{-0.05}$
N1	6.4970	XX	1s2s $^2p^4$ $^4P_{5/2}$	0.25	$0.16^{+0.05}_{-0.05}$

* Line labels for the inner-shell transitions follow Rudolph et al. (2013).

† Energy from Kramida & Ralchenko (1999) for the outer-shell and Rudolph et al. (2013) for the inner-shell transitions.

‡ Upper level of the transition. The lower level is the ground state of each ion.

§ Radiative branching ratio of the transition from the upper (k) to the lower (i) level. Note that $B_r(k, i) \equiv \frac{A_r(k, i)}{A_r(k) + A_a(k)}$ is different from the fluorescence yield $\omega_r(k) \equiv \frac{A_r(k)}{A_r(k) + A_a(k)}$, in which $A_x(k) = \sum_i A_x(k, i)$ for the fluorescence ($x = r$) and Auger ($x = a$) decay. The definitions and values for the inner-shell transitions are from Palmeri et al. (2003).

$^\parallel$ Line optical depth from the fitting.

5 Modeling

We conduct RT calculations (§ 5.1), present line ratio analyses (§ 5.2), and perform spectral fitting (§ 5.3).

5.1 Radiative transfer calculation

5.1.1 Setup

We used `ccloudy`, which is a numerical radiative transfer code based on the one-dimensional, static, and two-stream solver such as `xstar` (Kallman & Bautista 2001). It has been used in longer wavelengths in the past, but recent development has made the code applicable to high-resolution X-ray spectroscopy (Chakraborty et al. 2020a; Gunasekera et al. 2022). We used a release candidate of the version c25 (Gunasekera et al. 2024). For the atomic database, we used the `chianti` version 10.1 (Del Zanna et al. 2021).

For the setup (figure 4), we placed a point-like source at the origin for the incident emission. The emission has an X-ray luminosity (L_X) integrated over 1–1000 Ryd and a spectral shape of the disk blackbody with an innermost temperature of 2 keV, which best describes the observed continuum emission (§3.1). The photoionized plasma is represented by a slab and is characterized by three parameters: the ionization degree $\xi \equiv L_X/(nr_{in}^2)$ (erg cm s $^{-1}$) at the illuminated surface of the slab at a distance of r_{in} (cm) from the incident source (Tarter et al. 1969), the density n (cm $^{-3}$) constant over the slab, and the H-equivalent column density N_H (cm $^{-2}$) across the slab. We assumed no bulk or turbulent velocities. We ran the simulation with different settings for a grid of the three parameters logarithmically spaced at 0.1–0.5 dex. We hereafter quote their logarithmic values without physical units. We also assume that the electron and proton densities are the same for estimation.

For each grid, the code produces two spectra (figure 4). One is the transmitted spectrum through the photoionized plasma, in which absorption features are imprinted upon the incident contin-

uum emission. The other is the diffuse spectrum from the photoionized plasma caused by radiative deexcitation and recombination. Scattered emission also comes from the plasma due to electron scattering, which is not included; however, we can mimic this component by normalizing the incident emission independent of the energy by a factor of $e^{-N_H\sigma_{es}}$, in which σ_{es} is the electron scattering cross section. We made the multiplicative absorption model and the additive emission model based on the transmitted and diffuse spectrum, respectively (Porter et al. 2006), so that we can fit the spectra using the `xspec` fitting package (Arnaud 1996).

5.1.2 Results

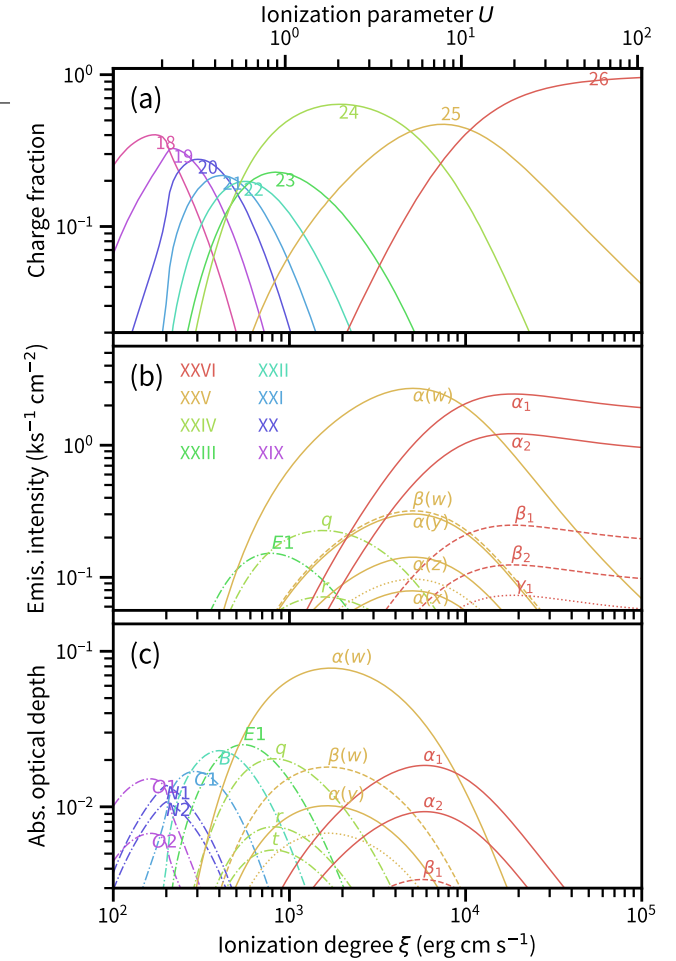


Fig. 5. (a) Charge fraction, (b) emission line intensity, and (c) absorption line optical depth of Fe as a function of the ionization degree ξ or the ionization parameter $U \equiv Q(H)/4\pi r^2 n c$, in which $Q(H)$ (s $^{-1}$) is the rate of H-ionizing photons calculated with `ccloudy` for $N_H = 10^{19.5}$ cm $^{-2}$. Emission line intensity is scaled assuming $r_{out} = 1.0 \times 10^{11} (N_H/10^{23.0})^{-0.5}$ cm and the distance to the source so as to approximately match with the observed flux. In (a), the fractions of the Fe $^{i+}$ ions are shown with an Arabic number $i \in \{18 \dots 26\}$, where $i = 26$ denotes fully-ionized Fe. In (b) and (c), conspicuous lines are shown with labels in table 3. Different colors are used for different Fe j feature with a Roman number $j \in \{XIX \dots XXVI\}$. Solid, dashed, and dotted curves are for $n = 4, 3, 2 \rightarrow 1$ transitions of outer-shell electrons, whereas dashed-and-dotted curves are for the $K\alpha$ transitions of inner-shell electrons. Alt text: three line plots of charge state distribution, emission intensity, and absorption depth as a function of the ionization degree.

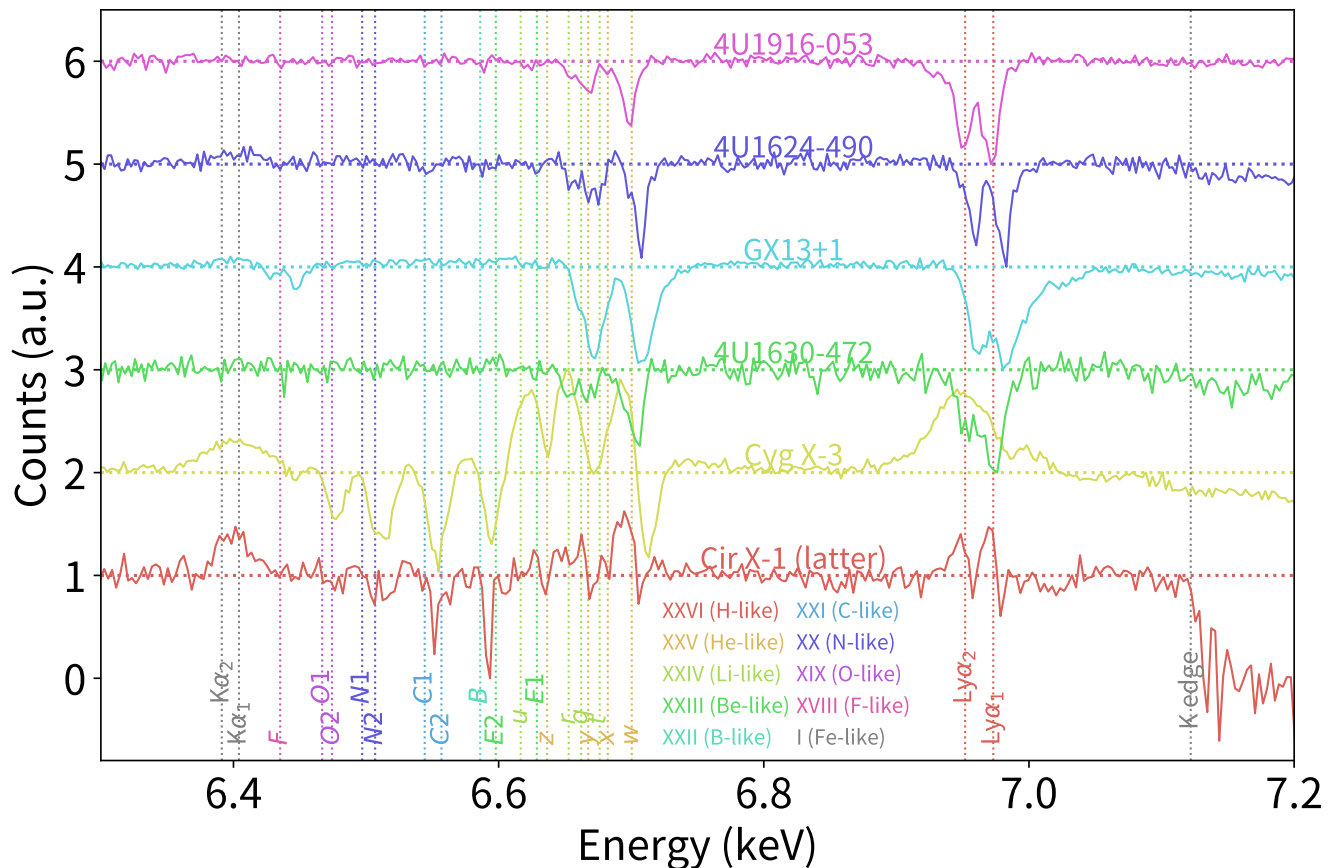


Fig. 6. Fe K-band spectra of some X-ray binaries observed with *Resolve*. Spectra are optimally-binned, detrended for the power-law continuum emission, scaled to ± 1 , and offset for clarity. We use the average spectra; all sources exhibit spectral variability, the details of which are described in individual papers (XRISM Collaboration et al. 2024; XRISM collaboration 2025; Miller et al. 2025). The rest-frame energies of Fe features are shown in different colors for Fe I (neutral), and XVIII (F-like) to XXIV (H-like). The labels follow Rudolph et al. (2013). The energy shift seen in most spectral features are real. Alt text: a line plot showing X-ray spectra of some X-ray binaries observed with *Resolve*.

Among the three parameters, ξ is the most important governing the charge and level populations and the formation of spectral features. We examined the calculation results for different ξ to compare to the observed spectra, focusing on the Fe emission and absorption features. Figure 5 shows the (a) charge fraction, (b) intensity of the emission lines, and (c) optical depth of the absorption lines as a function of ξ .

For the outer-shell transitions (Fe XXVI and XXV), the emission and absorption lines of the same spectral feature probe plasma in different ξ ranges. This is because the emission lines are mostly formed via recombination cascades, thus their intensity reflects the charge population that captures an electron; e.g., Fe XXVI Ly α emission intensity reflects the fully-ionized Fe $^{26+}$ ion population. In contrast, the absorption lines reflect the charge population that absorbs a photon of the energy; e.g., Fe XXVI Ly α absorption depth reflects the H-like Fe $^{25+}$ ion population. Forbidden lines such as Fe He α (z) are seen only in emission and not in absorption because the upper level is mostly populated by the recombination cascade or inner-shell photoionization.

For the inner-shell transitions (Fe XVIII to XXIV), the interpretation requires help from atomic physics theory and experiment. Their upper levels are mostly populated by photo-excitation or photo-ionization rather than by electron collision or by dielectronic recombination, as the electron temperature is too low to

cause the latter two processes. Therefore, many absorption features are formed at $\log \xi = 2-3$, at which mildly-ionized Fe ions are dominant (figure 5c). For elements of low atomic numbers, such photo-excited states decay predominantly by auto-ionization ejecting electrons (Auger process) rather than radiative deexcitation emitting photons (fluorescence). Therefore, they do not contribute for emission lines. For elements of high atomic numbers like Fe, however, the fluorescent decay becomes more dominant than the Auger decay, increasingly so for ions with a smaller number of electrons. Palmeri et al. (2003) conducted *ab initio* calculations of the Dirac equation for such Fe ions and derived the radiative branching ratio from various excited levels (table 3). The radiative branching ratio for the upper level of the Fe XXIV q line, for example, amounts to 1.00. Therefore, they contribute significantly for the emission lines, and can form a P Cygni profile similarly to outer-shell transitions. Such emission lines are indeed observed in a ground experiment (Rudolph et al. 2013). Mildly ionized Fe was collisionally ionized and trapped by an electron beam ion trap (EBIT) installed at a synchrotron facility, which provided a tunable, monochromatic photon beam that was passed through the ion cloud. Prominent emission lines such as Fe XXIV q , r , Fe XXIII $E1$ were observed as fluorescence decay of photo-excited states.

In photo-ionized plasmas around compact objects, these spectral features are predicted by the atomic physics and radiative

transfer combined, demonstrated by ground experiments, and are now observed in the X-ray microcalorimeter spectra of Cir X-1 having a wide range of $\log \xi = 2-4$ (figure 3). The uniqueness of Cir X-1 is better understood by inspecting other X-ray binaries with the Fe K features. We compared the spectra of Cyg X-3, 4U 1630-472, GX 13+1, 4U 1624-490, and 4U 1916-053 (sequence numbers 300065010, 900001010, 300036010, 300040010, and 300039010), which were also observed with *Resolve* as performance verification targets (figure 6). Cir X-1 and Cyg X-3 show (i) absorption features by both mildly and highly ionized Fe and (ii) emission features of highly ionized Fe, which are not the case for the other sources. Furthermore, Cir X-1 exhibits the Fe Ly α absorption at 7.0 keV as strong as the He α absorption at 6.7 keV. These characteristics are the consequences of having plasma in wide $\log \xi$ ranges. The presence of the deep absorption edge by Fe K α at 7.12 keV is also unique for Cir X-1.

5.2 Line ratio analysis

Before fitting the entire spectra, we estimate the plasma parameters using line ratios. This is a necessary step for identifying approximate values of the parameters; otherwise, the fitting often ends with a local minimum and ignores informative line ratios because the χ^2 statistics are dominated by spectral bins only with continuum emission that are more numerous. For the ξ values, we can constrain using the ratio between the He α and Ly α resonance lines of each element (§5.2.2). However, we should be aware that these lines, in particular Fe, are almost certainly optically thick as calculated in §1. Therefore, we first determine N_{H} (§5.2.1).

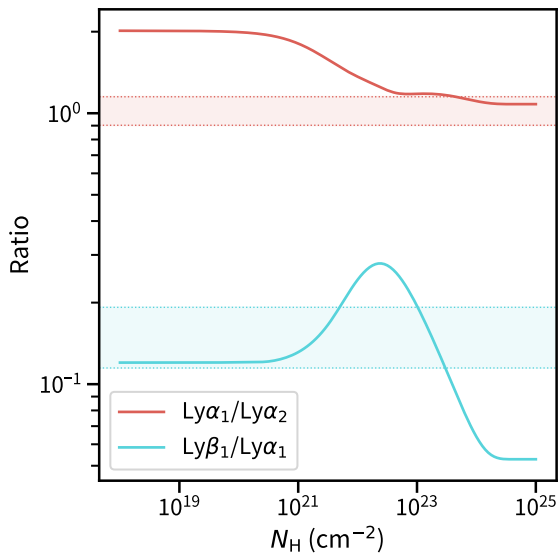


Fig. 7. Line ratio of the Fe Ly α doublet ($\text{Ly}\alpha_1/\text{Ly}\alpha_2$) and Lyman decrement ($\text{Ly}\beta_1/\text{Ly}\alpha_1$) as a function of N_{H} calculated for $\log \xi = 4.0$ (curves) and compared to the observed ratio (stripes) in the same colors. The M1 transition $2s^2S_{1/2} \rightarrow 1s^2S_{1/2}$ was blended into Ly α_2 . Alt text: a line plot showing the line intensity ratio as a function of the plasma thickness.

5.2.1 Column density

A novel technique was recently proposed (Gunasekera et al. 2025) using the Fe Ly α fine-structure doublet, which requires the spectral resolution of *Resolve*. The ratio of the two emission lines

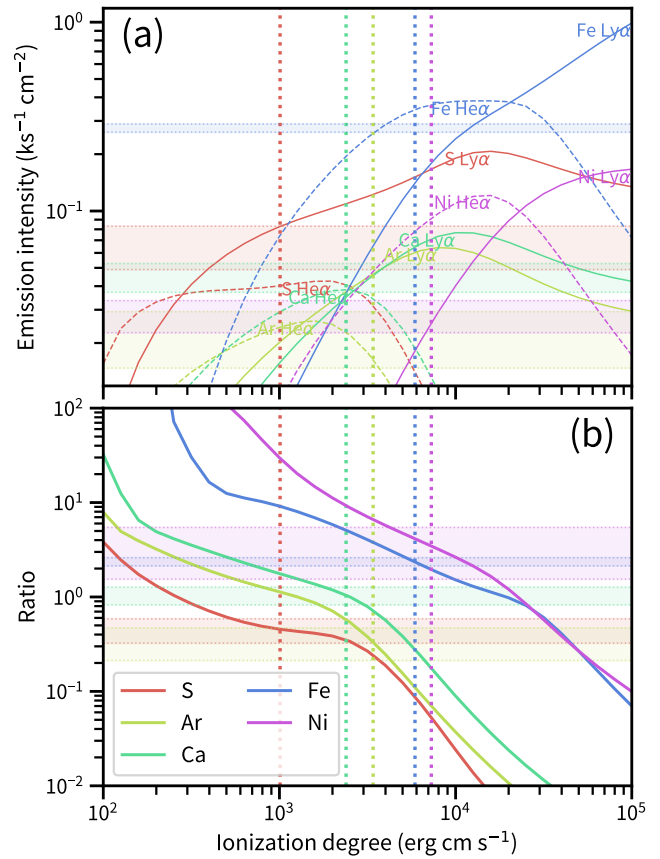


Fig. 8. (a) Emission line intensity as a function of ξ for the resonance lines of H-like (solid) and He-like (dashed) S, Ar, Ca, Fe, and Ni lines for $N_{\text{H}} = 10^{23}$ cm. The emission line is scaled in the same way as figure 5. The observed 1σ ranges of the He α (w) intensity are shown with the horizontal shades. (b) Line ratio of He α (w) and Ly α_1 as a function of ξ . The observed 1σ ranges of the line ratio are shown with the horizontal shades and their best matched ξ value is shown in (a) and (b) with the vertical dotted lines of the same color for each element. Alt text: two line plots showing emission line intensity and the intensity ratio of highly-ionized ions.

($\text{Ly}\alpha_1/\text{Ly}\alpha_2$) is 2 at the optically-thin limit for their statistical weights, which decreases toward 1 as the line optical depth increases, approaching the ratio of the source function at the depth where the line optical depth reaches $\sim 2/3$ seen from outside for each line (Barbier 1943). Figure 7 shows the result. Compared to the observation (table 2), we estimate $\log N_{\text{H}} \gtrsim 23$.

This can be further constrained using another pair of lines from the same ions (Chakraborty et al. 2020b) such as Ly β_1 over Ly α_1 , which is called the Lyman decrement in literature. The intensity ratio against N_{H} exhibits a non-monotonic curve. Similarly to the Ly α doublet ratio, the Lyman decrement approaches 1 as the line optical depth increases. However, it goes to the case D condition, in which a Lyman β photon degrades into a Balmer α photon and a Lyman α photon during their repeated resonance scattering. Therefore, the line ratio turns to a decreasing trend toward 0. By combining these diagnostics, we estimated $N_{\text{H}} \sim 23.5$.

5.2.2 Ionization degree

We next constrain ξ using the He α and Ly α line ratio for the given N_{H} . We used S, Ar, Ca, Fe, and Ni in the former half of the observation. Figure 8 (a) shows the expected line intensity based on

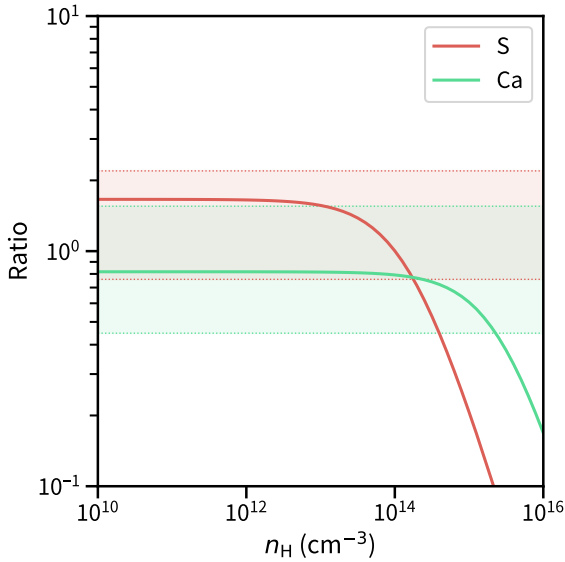


Fig. 9. R ratio of S and Ca $\text{He}\alpha$ complex calculated for $\log \xi = 3.2$ and $\log N_{\text{H}} = 22$. The observed ratios, using the entire dataset, are shown with stripes in the same color. Alt text: a line plot showing the R ratio as a function of plasma density.

the RT calculation. Figure 8 (b) shows the intensity ratio of the pair compared to the observation (table 2). We see that different elements trace different ranges of $\log \xi = 2.5 - 4.5$.

5.2.3 Plasma density

In collisionally-ionized plasmas (Gabriel & Jordan 1969), the $R \equiv I_z/(I_x + I_y)$ ratio is often used as a density diagnostic, in which I_x , I_y , and I_z are the intensity of the x , y , and z lines respectively in the $\text{He}\alpha$ line complex. The upper levels of x and y lines are populated due to excitation by proton and electron collisions and UV photon absorption from the upper level of z before it radiatively decays via a forbidden transition.

The R ratio serves as a density indicator even in photoionized plasmas where radiative processes dominate over collisional processes, but it is strongly affected by ξ and N_{H} (Porter & Ferland 2007). In practice, we should also be aware that the complex is often contaminated by other lines. To take Ar $\text{He}\alpha$ as an example, the z line blends with the S $\text{Ly}\beta$ line only at 3 eV away, which is serious considering the presence of the S $\text{Ly}\gamma$ line detected at a comparable intensity (figure 3b). We thus need to have the diagnostics based on dedicated RT calculation. We used less contaminated S and Ca $\text{He}\alpha$ complexes and used the sum of the former and the latter half of the spectrum for the sake of statistics. We obtained an upper limit $\log n \sim 14$ from S (figure 9) consistent with previous studies using the same technique (Schulz & Brandt 2002; Iaria et al. 2008).

5.3 Spectral fitting

We now have a good grasp of the plasma parameters through the line ratio analyses. We construct a spectral model to explain the observed spectra. We start with the former half of the spectrum to constrain the plasma by its emission. Upon the best-fit model for the continuum plus Fe $\text{K}\alpha$ fluorescence emission for the former half (§4.2.1), we added diffuse emission components of different ξ ,

Table 4. Physical model fitting result.

Comp*	$\log \xi$ (erg cm s^{-1})	$\log N_{\text{H}}$ (cm^{-2})	EM (10^{59} cm^{-3})	v^\dagger (km s^{-1})
emi1	$3.13^{+0.03}_{-0.03}$	$22.4^{+0.0}_{-0.1}$	2.0 ± 0.2	78^{+25}_{-10}
emi2	$4.60^{+0.06}_{-0.09}$	$24.2^{+0.2}_{-0.2}$	1.3 ± 0.3	337^{+19}_{-18}
abs1	$2.60^{+0.02}_{-0.01}$	$23.0^{+0.0}_{-0.0}$	—	-330^{+11}_{-7}
abs2	$4.34^{+0.23}_{-0.20}$	$22.4^{+0.2}_{-0.2}$	—	-272^{+18}_{-16}

* “emi1” and “emi2” are the components to explain the emission lines in the former half (figure 10a and 10b). “abs1” and “abs2” are the components to explain the absorption lines in the latter half (figure 10c).

† Energy shift from the fitting. The redward shift is positive.

N_{H} , emission measure (EM), and redshift (v) for the bulk motion. We note that N_{H} and EM can be determined independently as we can constrain N_{H} from the line ratios (figure 7). In the soft band (2.25–4.25 keV; figure 10a), a single component with $\log \xi = 3.2$ suffices to explain the S, Ar, and Ca emission lines.

In the hard band (6.45–8.5 keV; figure 10b), another component with a larger $\log \xi$ value is required to explain the Fe and Ni emission lines. To explain the Fe $\text{He}\alpha$ and Fe $\text{Ly}\alpha$ complex (insets in figure 10b), there are two solutions. One is to explain both features with a single $\log \xi \sim 3.7$ component as indicated in figure 8 (b). In this case, the two peaks in the $\text{Ly}\alpha$ complex and the three peaks in the $\text{He}\alpha$ complex are all explained by this component. The w , y , and z lines are for the three peaks in the $\text{He}\alpha$ complex, as initially guessed in table 2. The other is to explain the $\text{Ly}\alpha$ complex with the larger ξ component and the $\text{He}\alpha$ complex with the smaller ξ component. The w , q , and $E1$ lines are for the three peaks in the $\text{He}\alpha$ complex. We favor the latter, as the former requires different bulk velocities between the $\text{Ly}\alpha$ and $\text{He}\alpha$ lines of the same component. The best-fit parameters are given in table 4.

Finally, we used the latter half of the spectrum to constrain the plasma by its absorption. We focus on the 6.45–7.05 keV band, at which most absorption features are included. Upon the best-fit model for the continuum plus Fe $\text{K}\alpha$ fluorescence emission for the latter half (§4.2.1) and the emission line model for the former half (figure 10b), we multiplied the plasma absorption models. As is evident from the Fe $\text{Ly}\alpha$ line between the former and the latter half of the spectrum (figure 3c), the absorption by the plasma needs to be multiplied to the emission from the plasma. Two components with different ξ values explain the observed absorption features of Fe XIX–XXVI (figure 10c). The best-fit values are shown in table 4.

6 Discussion

We were successful in explaining the observed spectra with a physically motivated model based on the RT calculation. We now interpret this based on the picture in figure 4. We first discuss the cause of the observed X-ray variability in § 6.1. We then discuss the structure (§ 6.2) and dynamics (§ 6.3) of the outflow based on the parameters constrained by comparing the observation and RT calculations in § 5.

6.1 Covering materials

The variability of the former and the latter half of the spectrum is mostly attributable to the change of the normalization of the disk blackbody emission (table 1). There are two possibilities. One is that the intrinsic normalization of the emission has changed accordingly. The other is that the intrinsic normalization did not

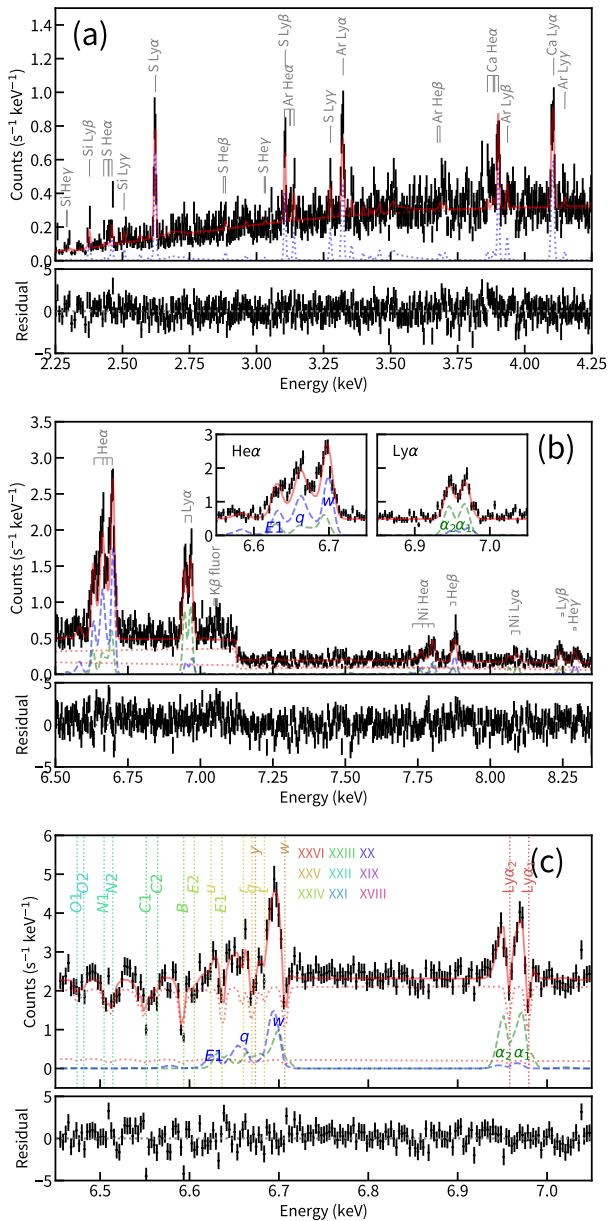


Fig. 10. Best-fit spectral model and data (upper panels) and the residuals (lower panels) for (a) former half, soft band, (b) former half, hard band, and (c) latter half, Fe $K\alpha$ band of the spectrum. Spectral model components are shown in solid (total), broken (transmitted and scattered), or dashed (diffuse) curves. Blue and green curves are respectively for the “emi1” and “emi2” component in table 4. The line labels are shifted by the best-fit Doppler velocity. Alt text: three line plots showing X-ray spectra and best-fit models.

change much, but the fraction of coverage by a very thick material in the line of sight has changed. The material is so thick ($\gtrsim 10^{26} \text{ cm}^{-2}$) that almost no emission comes out in the *Resolve* energy band. We consider the latter to be the case for three reasons. One is that the scattered emission, which we consider to be the origin of the continuum emission below ~ 4 keV, did not change. If the intrinsic normalization of the incident emission had changed, the scattered emission would have changed proportionally. The second is that the best-fit normalization of the disk blackbody emission is too small. For the face value of $N^{(\text{disk})} = 16$ (table 1) at a 9.4 kpc distance and $\theta = 75$ degree, the inner disk radius is $R_{\text{in}} = 7.7$ km, which is smaller than the typical NS radius (Miller et al. 2019). The third is that we see both emission and absorption features in the latter half of the spectrum. If we had observed all the incident emission, the transmitted emission through the plasma should overwhelm the diffuse emission from the plasma, and we would have observed a spectrum predominantly characterized by absorption features. This is the situation for the four sources from the top in figure 6.

In the former half, the thick material blocked a significant fraction of the incident emission, and the diffuse emission dominates. This is akin to the situation of X-ray binaries during eclipses or deep dips. Indeed, high-resolution X-ray spectra of such sources are dominated by emission lines with little absorption features (Schulz et al. 2002; Hirsch et al. 2019; Pradhan & Tsujimoto 2024), as we saw in figure 3 (a).

When the thick material goes out of the line of sight, the dip phase ends (figure 1 inset), and we observe the entire intrinsic normalization of the incident emission, which is assessed as $N^{(\text{disk})} \sim 40$ at the peak with the NICER spectrum (Tominaga et al. 2023). This corresponds to $7.6 \times 10^{37} \text{ erg s}^{-1}$ in 1–1000 Ryd. The scattered emission (table 1) has $\sim 1\%$ of the intrinsic incident luminosity, suggesting that the optical depth of electron scattering is $\sim 10^{-2}$, so $N_{\text{H}} \sim 10^{-2}/\sigma_{\text{es}} = 10^{23} \text{ cm}^{-2}$. This is in reasonable agreement with the estimate from the line ratio analysis (§ 5.2.1).

The putative thick ($\gtrsim 10^{26} \text{ cm}^{-2}$) material and the observed PCA are in the line of sight only during the dip phase along the orbital phase. The most likely entity for them is the hot spot formed at the position where the accreting matter lands on the accretion disk (figure 4). It may have some bimodal density structure along its radius responsible for both the thick material and the PCA.

6.2 Structure of outflow

We constrain the system parameters for the geometry in figure 4. The inner radius is estimated as $r_{\text{in}} = \sqrt{L_{\text{X}}/n\xi} = 9 \times 10^{10} n_{12} \text{ cm}$, in which n_{12} is the density in the unit of 10^{12} cm^{-3} . Then, $r_{\text{out}} = r_{\text{in}} + N_{\text{H}}/n = (0.9n_{12}^{-1/2} + n_{12}^{-1}) \times 10^{11} \text{ cm}$. This is in reasonable agreement with the scaling used in figures 5 and 8 to match the RT calculation with the observed line flux. This is a minimum estimate of r_{out} by the assumption that the volume filling factor is unity for the spherically symmetric assumption. We do not know the outer radius of the accretion disk, but it should be smaller than the effective Roche-lobe radius of the binary of 10^{12} cm (Eggleton 1983). From these estimates, the launching radius of the outflowing plasma is close to the outer edge of the accretion disk. No substantial photoionized plasma is present much closer to the NS than this, as we would otherwise have observed the Fe $\text{Ly}\alpha$ emission line stronger than He α for a larger ξ by recombination of Fe^{26+} ions (figures 3c and 8). Likewise, no substantial plasma is present much farther than this, as we would otherwise have observed deeper absorption lines of Fe XIX (O1, O2) than those of

Fe XX ($N1$, $N2$) and Fe XXI ($C1$, $C2$) for a smaller ξ (figures 5c and 10c).

6.3 Dynamics of outflow

The Eddington luminosity for a $1.4 M_{\odot}$ NS is $L_{\text{Edd}} = 1.8 \times 10^{38} \text{ erg s}^{-1}$. At the time of the present observation, Cir X-1 was at a sub-Eddington luminosity $L_X = 7.6 \times 10^{37} \text{ erg s}^{-1} \sim 0.4L_{\text{Edd}}$ (§ 4.2.1), but an outflowing wind was observed with a peak-to-valley distance in the P Cygni profile of $\sim 5 \times 10^2 \text{ km s}^{-1}$ (§ 4.2.2 and § 4.2.3). One would naturally expect that the line photons contribute for the outward radiative force in addition to the continuum photons. The enhancement is described by the radiative force multiplier $\mathcal{M} \equiv (\sigma_{\text{es}} + \langle \sigma_{\text{line}} \rangle) / \sigma_{\text{es}}$, in which $\langle \sigma_{\text{line}} \rangle$ is the cross section of line photon interactions averaged over wavelengths weighted by the incident spectral shape (Tarter & McKee 1973). The Eddington luminosity is effectively reduced by $L_{\text{Edd}} / \mathcal{M}$. \mathcal{M} decreases as ξ increases because more electrons are stripped from the ions. This is in line with the observation, in which the blue-shifted velocity of $330_{-11}^{+7} \text{ km s}^{-1}$ for the smaller ξ component is significantly faster than that of $272_{-18}^{+16} \text{ km s}^{-1}$ for the larger ξ component (table 4).

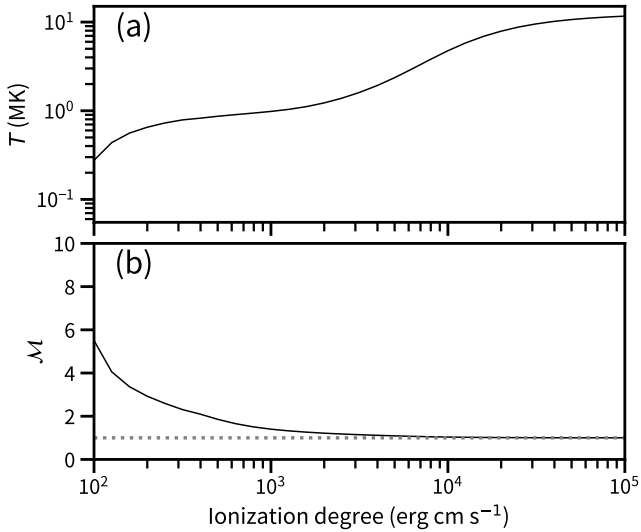


Fig. 11. (a) Plasma temperature (T) and (b) force multiplier \mathcal{M} as a function of ξ based on the RT calculation.

We can derive $\mathcal{M}(\xi)$ based on the presented RT calculation using *cLOUDY*, as we have solved all the photon-matter interaction and verified it with the observed X-ray spectra. Figure 11 shows $\mathcal{M}(\xi)$ as well as the plasma temperature $T(\xi)$ at which the heating and cooling balance. The observed bulk velocity is larger than the sound velocity for the plasma temperature, and the Sobolev condition holds for the line force to work efficiently. The general trend of $\mathcal{M}(\xi)$ is the same as the classical work by Tarter & McKee (1973) among variations of incident spectral shapes. For our setup of the disk blackbody emission representative of LMXBs, $\mathcal{M}(\xi) > 3$ at $\log \xi < 2.1$, which makes the observed L_X to exceed $L_{\text{Edd}} / \mathcal{M}(\xi)$ and can give rise to radiatively-driven outflow. The faster component with a smaller ξ may drag the slower component with a larger ξ if they spatially coexist. For the disk wind, we would also expect that the centrifugal force outward also works to offset the gravitational force inward. Therefore, we argue that the radiative force by continuum and line photons is suf-

ficient to produce the observed outflowing plasma. The total mass loss rate, if radially symmetric, is estimated as $4\pi r_{\text{out}}^2 n m_p v \approx 2 \times 10^{-7} (1 + 0.9\sqrt{n_{12}}) M_{\odot} \text{ yr}^{-1}$.

7 Conclusion

The new era of high-resolution X-ray spectroscopy with X-ray microcalorimeters has begun. Most spectral features in plasmas around compact objects are formed in NLTE conditions, and thus RT calculation is required to interpret the data. We presented such a study for a LMXB using *cLOUDY* focusing on line ratio analysis.

Many new spectral features, both emission and absorption, were detected with *Resolve* from Cir X-1 at $\phi_{\text{orb}} = 0.926 - 0.973$. The X-ray spectra changed drastically in the former and the latter half of the observation, which was explained by the apparent change in the continuum emission. The diffuse and scattered emission from the photoionized plasma remained unchanged, suggesting that the X-ray variability across the orbital phase is caused by the local intervening matter on the accretion disk as proposed by Tominaga et al. (2023).

We constrained the plasma parameters ($\log \xi = 2.5 - 4.5$, $\log N_{\text{H}} \sim 23$, and $\log n \lesssim 14$) using the line ratio analysis. These values are consistent with the independent estimates using the electron scattering optical depth and absolute line flux. We further derived the outward velocity ($\sim 300 \text{ km s}^{-1}$) of the plasma and its distance from the NS as $\mathcal{O}(10^{11} \text{ cm})$, based on which we argue that the launching radius of the outflowing plasma is close to the outer edge of the accretion disk. We further calculated the radiative force multiplier based on the RT calculation and argue that the radiative force, including the line force contribution, is sufficient to drive the observed outflow at a sub-Eddington luminosity.

Acknowledgments

The authors appreciate Gary J. Ferland at the University of Kentucky, Chamani M. Gunasekera at STSci, Peter van Hoof at the Royal Observatory of Belgium, and Stephano Bianchi at Università degli Studi Roma Tre for their efforts to make *cLOUDY* useful for X-ray spectroscopy as presented here and their expertise advice since a *cLOUDY* summer school held at ISAS in 2024. We also appreciate Mayu Tominaga for her contribution in scientific justification of this performance verification program and observation planning through her thesis. We thank all those who contributed to the XRISM mission. This work was supported by the JSPS Core-to-Core Program (grant number: JPJSCCA20220002). MS acknowledges support by Grants-in-Aid for Scientific Research 19K14762 and 23K03459 from the Ministry of Education, Culture, Sports, Science, and Technology (MEXT) of Japan. Part of this work was performed under the auspices of the U.S. Department of Energy by Lawrence Livermore National Laboratory under Contract DE-AC52-07NA27344. The material is based upon work supported by NASA under award number 80GSFC21M0002. This research made use of the JAXA's high-performance computing system JSS3.

References

- Arnaud, K. A. 1996, in *Astronomical Data Analysis Software and Systems V*, ed. G. Jacoby & J. Barnes, Vol. 101, 17,
- Asai, K., Mihara, T., Matsuoka, M., et al. 2014, *PASJ*, 66, 1,
- Barbier, D. 1943, *Annales d'Astrophysique*, 6, 113

- Bautista, M. A., Mendoza, C., Kallman, T. R., & Palmeri, P. 2004, *A&A*, 418, 1171,
- Behar, E., & Netzer, H. 2002, *ApJ*, 570, 165,
- Boutloukos, S., van der Klis, M., Altamirano, D., et al. 2006, *ApJ*, 653, 1435,
- Brandt, W. N., Fabian, A. C., Dotani, T., et al. 1996, *MNRAS*, 283, 1071,
- Brandt, W. N., & Schulz, N. S. 2000, *ApJ*, 544, L123,
- Canizares, C. R., Davis, J. E., Dewey, D., et al. 2005, *PASP*, 117, 1144,
- Chakraborty, P., Ferland, G. J., Bianchi, S., & Chatzikos, M. 2020a, *Res. Notes AAS*, 4, 184,
- Chakraborty, P., Ferland, G. J., Chatzikos, M., Guzmán, F., & Su, Y. 2020b, *ApJ*, 901, 69,
- . 2021, *ApJ*, 912, 26,
- Del Zanna, G., Dere, K. P., Young, P. R., & Landi, E. 2021, *ApJ*, 909, 38,
- Doyle, T. F., Holland, M. P., Hill, R. S., et al. 2022, *Proc. of SPIE*, 12181, 1495,
- Eggleton, P. P. 1983, *ApJ*, 268, 368,
- Foster, A. R., & Heuer, K. 2020, *Atoms*, 8, 49,
- Fuhr, J. R., Martin, G. A., & Wiese, W. L. 1988, *Journal of Physical and Chemical Reference Data*, 17
- Gabriel, A. H., & Jordan, C. 1969, *MNRAS*, 145, 241,
- Gendreau, K. C., Arzoumanian, Z., Adkins, P. W., et al. 2016, *Proc. of SPIE*, 9905, 99051H,
- Gunasekera, C. M., Chatzikos, M., & Ferland, G. J. 2022, *Astronomy*, 1, 255,
- Gunasekera, C. M., van Hoof, P. A. M., Chatzikos, M., & Ferland, G. J. 2024, *ApJ*, submitted,
- Gunasekera, C. M., van Hoof, P. A. M., Tsujimoto, M., & Ferland, G. J. 2025, *A&A*, 694, L13,
- Heinz, S., Sell, P., Fender, R. P., et al. 2013, *ApJ*, 779, 171,
- Heinz, S., Burton, M., Braiding, C., et al. 2015, *ApJ*, 806, 265,
- Hirsch, M., Hell, N., Grinberg, V., et al. 2019, *A&A*, 626, A64,
- Hölzer, G., Fritsch, M., Deutsch, M., Härtwig, J., & Förster, E. 1997, *PRA*, 56, 4554,
- Iaria, R., D’Ai, A., Lavagetto, G., et al. 2008, *ApJ*, 673, 1033,
- Iaria, R., Di Salvo, T., Burderi, L., & Robba, N. R. 2001, *ApJ*, 561, 321,
- Ishisaki, Y., Kelley, R. L., Awaki, H., et al. 2022, *Proc. of SPIE*, 12181, 409,
- Jonker, P. G., Nelemans, G., & Bassa, C. G. 2007, *MNRAS*, 374, 999,
- Kallman, T., & Bautista, M. 2001, *The Astrophysical Journal Supplement Series*, 133, 221,
- Kallman, T. R., Palmeri, P., Bautista, M. A., Mendoza, C., & Krolik, J. H. 2004, *ApJS*, 155, 675,
- Kaluźniński, L. J., Holt, S. S., Boldt, E. A., & Serlemitsos, P. J. 1976, *ApJ*, 208, L71,
- Kilbourne, C. A., Sawada, M., Tsujimoto, M., et al. 2018, *PASJ*, 70, 18,
- Kinkhabwala, A., Sako, M., Behar, E., et al. 2002, *ApJ*, 575, 732,
- Kramida, A., & Ralchenko, Y. 1999, *NIST Atomic Spectra Database, NIST Standard Reference Database 78*, National Institute of Standards and Technology,
- Margon, B., Lampton, M., Bowyer, S., & Cruddace, R. 1971, *ApJ*, 169, L23,
- Matsuoka, M., Kawasaki, K., Ueno, S., et al. 2009, *PASJ*, 61, 999,
- Menzel, D. H., & Baker, J. G. 1937, *ApJ*, 86, 70,
- Midooka, T., Tsujimoto, M., Kitamoto, S., et al. 2021, *JATIS*, 7, 028005,
- Mihara, T., Nakajima, M., Sugizaki, M., et al. 2011, *PASJ*, 63, S623,
- Miller, M., J., Mizumoto, M., & Shidatsu, M. 2025, *PASJ*, submitted
- Miller, M. C., Lamb, F. K., Dittmann, A. J., et al. 2019, *ApJL*, 887, L24,
- Mitsuda, K., Inoue, H., Koyama, K., et al. 1984, *PASJ*, 36, 741
- Mizumoto, M., Tsujimoto, M., Cumbee, R., et al. 2022, *Proc. of SPIE*, 12181, 1479,
- Mochizuki, Y., Tsujimoto, M., Kilbourne, C. A., et al. 2024, *Proc. of SPIE*, 13093, 1686,
- Nicolson, G. D. 2007, *ATel*, 985, 1
- Palmeri, P., Mendoza, C., Kallman, T. R., & Bautista, M. A. 2003, *A&A*, 403, 1175,
- Parkinson, P. M. S., Tournear, D. M., Bloom, E. D., et al. 2003, *ApJ*, 595, 333,
- Porter, F. S., Chiao, M. P., Eckart, M. E., et al. 2016, *JLTP*, 184, 498,
- Porter, R. L., & Ferland, G. J. 2007, *ApJ*, 664, 586
- Porter, R. L., Ferland, G. J., Kraemer, S. B., et al. 2006, *PASP*, 118, 920,
- Pradhan, P., & Tsujimoto, M. 2024, *Bulletin de la Société Royale des Sciences de Liège*, in press
- Rudolph, J. K., Bernitt, S., Epp, S. W., et al. 2013, *PRL*, 111, 103002,
- Schulz, N. S., & Brandt, W. N. 2002, *ApJ*, 572, 971,
- Schulz, N. S., Canizares, C. R., Lee, J. C., & Sako, M. 2002, *The Astrophysical Journal*, 564, L21,
- Schulz, N. S., Kallman, T. E., Galloway, D. K., & Brandt, W. N. 2008, *ApJ*, 672, 1091,
- Shipman, R. F., Kitamoto, S., Wolfs, R., et al. 2024, *Proc. of SPIE*, 13093, 1617,
- Shirey, R. E., Bradt, H. V., Levine, A. M., & Morgan, E. H. 1998, *ApJ*, 506, 374,
- Shirron, P. J., Kimball, M. O., Ottens, R. S., et al. 2024, *Proc. of SPIE*, 13093, 1653,
- Smith, R. K., Brickhouse, N. S., Liedahl, D. A., & Raymond, J. C. 2001, *ApJ*, 556, L91,
- Tanaka, K. 1986, *PASJ*, 38, 225
- Tarter, C. B., & McKee, C. F. 1973, *ApJ*, 186, L63,
- Tarter, C. B., Tucker, W. H., & Salpeter, E. E. 1969, *ApJ*, 156, 943,
- Tashiro, M. S., Maejima, H., Toda, K., et al. 2020, *Proc. of SPIE*, 11444, 176,
- Tennant, A. F., Fabian, A. C., & Shafer, R. A. 1986, *MNRAS*, 219, 871,
- Tominaga, M. 2024, PhD thesis, University of Tokyo
- Tominaga, M., Tsujimoto, M., Ebisawa, K., Enoto, T., & Hayasaki, K. 2023, *ApJ*, 958, 52,
- Tsujimoto, M., Mizumoto, M., Ebisawa, K., Odaka, H., & Wada, Q. 2024, *ApJ*, 960, 46,
- van der Klis, M. 2006, in *Compact Stellar X-ray Sources*, 1st edn., ed. W. Lewin & M. Van Der Klis (Cambridge University Press), 39–112,
- Weisskopf, M. C., Tananbaum, H. D., Speybroeck, L. P. V., & O’Dell, S. L. 2000, *Proc. of SPIE*, 4012, 2,
- Wilms, J., Allen, A., & McCray, R. 2000, *ApJ*, 542, 914,
- Wojdowski, P. S., Liedahl, D. A., Sako, M., Kahn, S. M., & Paerels, F. 2003, *ApJ*, 582, 959,
- XRISM collaboration. 2025, *Nature*, submitted
- XRISM Collaboration, Audard, M., Awaki, H., et al. 2024, *ApJL*, 977, L34,
- Yerokhin, V. A., & Surzhykov, A. 2019, *Journal of Physical and Chemical Reference Data*, 48, 033104,